ChemPubSoc Europe

DOI: 10.1002/open.201800201

Open Access ChemistryOPEN Full Papers

SBA15–Fluconazole as a Protective Approach Against Mild Steel Corrosion: Synthesis, Characterization, and Computational Studies

Victoria Bustos-Terrones,*[a] Iris N. Serratos,[a] Rubicelia Vargas,[a] Bruno C. Landeros-Rivera,[a] Yaneth A. Bustos-Terrones,[b] Ana M. Soto Estrada,[a] Jonathan O. Vicente Escobar,[a] Mario A. Romero Romo,[c] Jorge Uruchurtu,[d] Carmina Menchaca,[d] Juan M. Esparza Schulz,[a] and Armando Domínguez[a]

A SBA15–Fluconazole composite (SBA15-Flu) was prepared to formulate a self-healing coating for mild steel. The composite was obtained by dispersing SBA15 in a methanolic solution containing Fluconazole (Flu). The materials were characterized by using different techniques. Electrochemical impedance spectroscopy (EIS) was used for protective behavior evaluation of the coatings on mild steel substrates in an electrolytic solution prepared from sodium chloride and ammonium sulfate. The EIS results indicate that the inhibitor trapped in the SiO_2 matrix is released when it comes into contact the aggressive solution, thus protecting the metal. To understand the inhibitor release mechanism, docking studies were used to model the SBA15-Flu complex, which allowed us to further determine polar and non-polar contributions to the binding free energy. An analysis of the electron density within the quantum theory of atoms in molecules and the non-covalent interaction index frameworks were also carried out for the most favorable models of SBA15-Flu. The results indicate that the liberation rate of the Flu molecules is mainly determined by the formation of strong O–H···O, O–H···N, and O–H···F hydrogen bonds.

1. Introduction

Recently, derived from the quest for corrosion inhibitor materials that comply with current environmental legislation, self-healing or self-repairing coatings have attracted the attention of several research groups, who have developed and evaluated different systems, including metallic films,[1–3] conversion[4,5] and ceramic layers,[6–8] polymers,[9] porous materials,[10–12] and composite materials, among others. This kind of coating has an essential characteristic: it responds to external stimuli such as changes in temperature, pH, as well as chemical and mechanical damages, restoring their original properties and protective behavior. The first self-healing coatings, synthesized by White et al.,[13] consisted of polymeric films with microcontainers filled with the same monomers of the polymeric matrix, capable of autonomously curing their cracks. This material incorporates a microencapsulated healing agent that is released after some damage or mechanical deformation of the polymer.

The barrier properties of damaged coatings can also be recovered through the simple blocking of defects by adding insoluble precipitates.[14] Shchukin and co-workers[15–18] evaluated several self-healing systems, including halloysite nanopores, titanium oxide nanoparticles, and silicon oxide, as reservoirs of a corrosion-inhibiting agent, with sensitivity to pH changes. Snihirova et al.,[19] studied the self-healing properties of several films. To protect aluminum 2024, they dispersed microparticles

[a] Dr. V. Bustos-Terrones, Dr. I. N. Serratos, Dr. R. Vargas, Dr. B. C. Landeros-Rivera, Prof. A. M. Soto Estrada, J. O. Vicente Escobar, Dr. J. M. Esparza Schulz, Dr. A. Domínguez
Departamento de Química
Universidad Autónoma Metropolitana-Iztapalapa
San Rafael Atlixco 186, Col. Vicentina
Ciudad de México, C.P. 09340 (Mexico)
E-mail: victoriabt@xanum.uam.mx

[b] Dr. Y. A. Bustos-Terrones
División de Estudios de Posgrado e Investigación—Ingeniería Ambiental
Instituto Tecnológico de Culiacán
Juan de Dios Batiz 310, Col. Guadalupe
Culiacán, Sinaloa C.P. 80220 (Mexico)

[c] Dr. M. A. Romero Romo
Área Ingeniería de Materiales
Universidad Autónoma Metropolitana-Azcapotzalco
Av. San Pablo 180, Col. Reynosa, Ciudad de México, C.P. 02200 (Mexico)

[d] Dr. J. Uruchurtu, Dr. C. Menchaca
Universidad Autónoma del Estado de Morelos
Centro de Investigación en Ingeniería y Ciencias Aplicadas
Av. Universidad 1009, Col. Chamilpa
Cuernavaca, Morelos C.P. 60010 (Mexico)

Supporting Information and the ORCID identification number(s) for the author(s) of this article can be found under: https://doi.org/10.1002/open.201800201.

of hydroxyapatite doped with cerium molybdate in an hybrid silica–zirconia sol-gel film.[19] Other kind of additives, layered double hydroxides, and cerium molybdate hollow nanospheres loaded with mercaptobenzothiazole, as an inhibitor, were mixed in epoxy primers and studied as self-healing systems on galvanized steel and aluminum 5083.[20,21] These self-healing coatings respond to pH changes and to the presence of chloride ions. Hallosytes, another kind of porous material, have been evaluated as containers of organic compounds for mild steel anticorrosion protection in acid media, with promising results.[22–24]

Among the mesoporous materials, SBA15 (SiO_2) is well known for a wide variety of applications in fields such as biology,[25] chemistry,[26] electrochemistry,[27–29] and medicine, where it has been used as a controlled drug-delivery system.[30–40] SBA15 materials have high volumes (up to 1 $cm^3 g^{-1}$) and elevated specific surface areas (around 1000 $m^2 g^{-1}$), allowing the adsorption of a variety of substances in their narrow channels (2–50 nm diameter), which are released under suitable environments. This property of SBA15 and the advances reported in this field suggest a starting point for the preparation of a composite material as part of the formulation of a coating with self-healing characteristics. Ávila-González et al.[41] evaluated the protective behavior of a "smart" layer on mild steel substrates in a 3% wt NaCl solution; the film was formulated by dispersing 5% wt of SBA15 loaded with $Fe(NO_3)_3$ particles, which act as mild steel corrosion inhibitor; the rust rate was reduced 100-fold compared to the case where the coating was prepared without an inhibitor.

Recently, our group described evidence of anticorrosion protection of fluconazole (Flu) on mild steel in a pH solution close to neutral. The results demonstrated that the best inhibitor concentration was 150 ppm, which maintained its effect even after 8 days.

This work focuses on the synthesis, preparation, and electrochemical evaluation of a protective coating (with self-healing features) containing a composite material, a SiO_2 matrix, in which pores the inhibitor molecule is trapped. When some external effects or the environmental conditions damage the coating, Flu is released and fulfills its function as a mild steel corrosion inhibitor. Electrochemical impedance spectroscopy was used to evaluate the protective behavior of the prepared liners. Besides, in silico studies to correlate the experimental findings are presented. The docking studies consider the MCM-41 layer model,[42] taking into consideration that the MCM-41 is a silica homologous to the SBA15 with a pore-size distribution of 2–5 nm (microporous matrix). Three cases were simulated computationally: the interactions between 1) the surface of SBA15 containing internal hydroxyls with Flu (SF1); 2) the inner pore of SBA15 (considering hydroxyl groups too) with Flu (SF2); and 3) hydroxylated-free SBA15 with Flu (SF3). For each case, the polar (ΔG_p) and nonpolar (ΔG_{np}) contributions to the binding free energy (ΔG_b) were determined, using the adaptive Poisson–Boltzmann program (APBS). ΔG_b was favorable in all cases; consequently, a study of the intermolecular interactions responsible for the SBA15-Flu complex formation was carried out through analysis of the electron density obtained from density functional theory (DFT) computations. For this purpose, the quantum theory of atoms in molecules (QTAIM),[43] and the non-covalent interactions index (NCI)[44] were both employed, as they have proven to be useful for the understanding and characterization of weak interactions.

This work contributes to understanding the controlled release mechanism of substances when a SBA15 porous matrix is used as the delivery system. This knowledge is important not only for smart coating in corrosion science, but also for biological and pharmacological applications.

2. Results and Discussion

2.1. Materials Characterization

The TEM images shown in Figure 1 confirm the 2D hexagonal structure of the porous SBA15 material.[45] The cylindrical pores of the material have an average pore diameter of approximately 7.3 nm. Figures 1a and 1b display the top view of the pores arrangement (SBA15 porous matrix and SBA15-Flu composite, respectively) where the pores entries of the pores are distinguished. The pore diameter reduction from 7.3 to 3.5 nm in pore diameter caused by the adsorption of Flu molecules on the surface and inside the porous of the matrix, can be observed in Figure 1b. To confirm the existence and distribution of Flu in the structure of the SBA15-Flu composite, energy dispersive spectroscopic (EDS) mapping was used (Figure 1c).

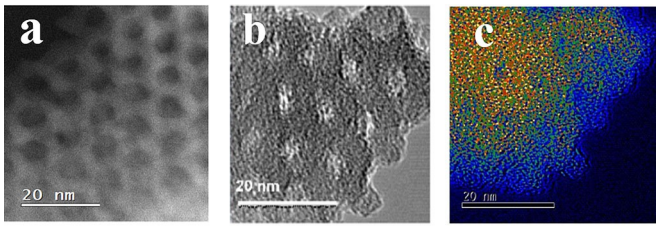

Figure 1. TEM images of a) the SBA15 matrix and b) the SBA15-Flu composite with 3:1 weight ratio; c) EDS characterization of the SBA15-Flu structure: nitrogen and fluorine atoms are represented green and orange, respectively.

The characteristic reflections for SBA15 material (2D hexagonal mesoporous structure), before and after loading Flu, can be observed in Figure 2. The diffraction lines in both the SBA15 porous matrix and SBA15-Flu appear at the same values of 2θ, indicating that the presence of Flu does not change the structure of the porous matrix. The XRD pattern for the crystals of Flu can be seen in the inset. These results are consistent with those reported by Papageorgiou et al.,[46] and Obaidat et al.[47]

Figure 3 depicts nitrogen adsorption–desorption isotherm of the SBA15 porous matrix (lines in dark blue), where a type IVa adsorption isotherm is observed (IUPAC classification),[48] which is associated with mesoporous materials such as SBA15. These results are consistent with those reported by Huang et al.[49] The synthesized material presents a high specific surface area (657 $m^2 g^{-1}$). On the other hand, to verify the Flu entrapment

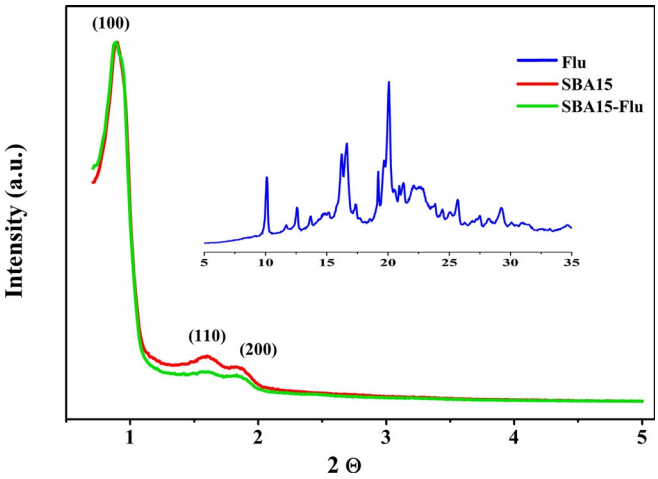

Figure 2. XRD (small angle X-ray scattering: from $2\theta = 0$ to 5). SBA15 matrix (red line) and SBA15 after the adsorption of Flu (green line); inset blue line corresponds to the Flu diffraction line.

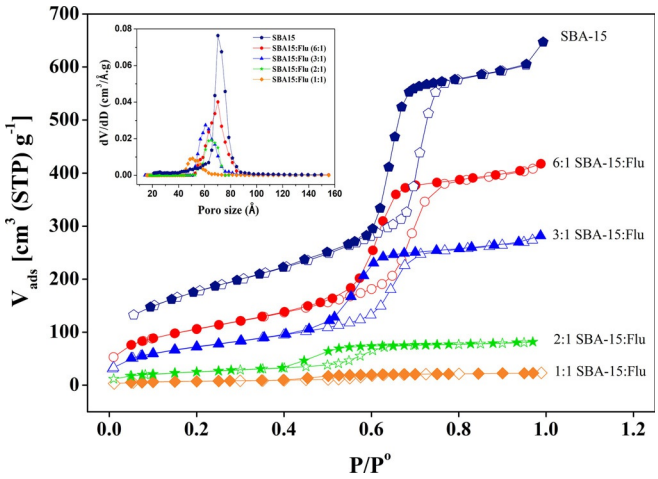

Figure 3. Nitrogen adsorption–desorption isotherms and pore-size distribution for the SBA15 matrix and SBA15 after adsorbing different concentrations of Flu (SBA15-Flu composites). The inset shows the pore-size distribution functions for the prepared composites.

in the porous matrix, physical nitrogen adsorption analyses were performed on the composites prepared with the 6:1, 3:1, 2:1, and 1:1 SBA15-Flu weight ratios. The same figure shows the unimodal pore-size distribution (inset) calculated by using non-localized density functional theory (NLDFT) for the desorption curves;[49] the textural parameters of the prepared materials are shown in Table 1.

Figure 3 also displays the resulting isotherms (type IVa with a hysteresis loop type H1). As expected, the amount of N_2 adsorption decreased as the concentration of Flu dispersed in the mesoporous matrix increased, suggesting that the drug moves into the pores of the material, as indicated by the decrease in the hysteresis loop as well as the diminution of the pore diameter. These pore-size distribution functions are presented in the inset.

Table 1. BET surface area (A_{BET}) and pore-size distribution (D_{NLDF}) of the SBA15 porous matrix and the composite SBA15-Flu at different weight ratios (6:1, 3:1, 2:1, and 1:1).

Sample	SBA15	SBA15-Flu[a] 6:1	SBA15-Flu[a] 3:1	SBA15-Flu[a] 2:1	SBA15-Flu[a] 1:1
A_{BET} [$m^2 g^{-1}$]	657	384	265	92	27
D_{NLDF} [nm]	7.3	7.0	6.1	5.1	3.5

[a] Weight ratio.

Figure 4 shows the corresponding FTIR spectra of the surface composition of the materials. The spectrum of SBA15 matrix (red line) depicts the signals at 805 and 970 cm^{-1},

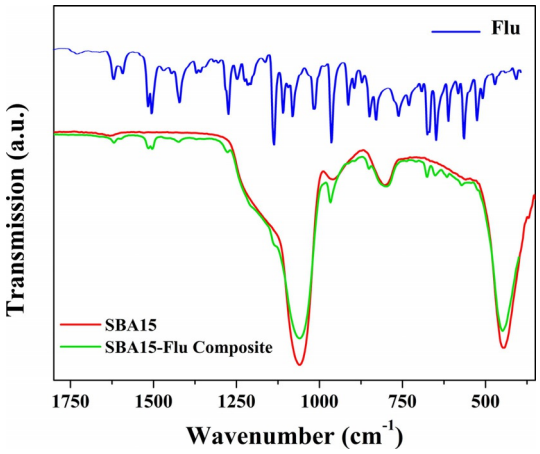

Figure 4. FTIR spectra of the materials: Fluconazole (Flu) and the SBA15 porous matrix before and after the adsorption of Flu.

which can be attributed to antisymmetric and symmetric stretching vibrations of Si–OH bonds, and at 1060 and 446 cm^{-1}, which correspond to stretching vibrations of Si-O–Si bonds. The main vibrational frequencies of the functional groups present in the Flu molecule can be observed in the blue spectrum (C–F stretching around 1125 and 1260 cm^{-1}, aromatic C=C stretching at 1515 cm^{-1}, and aromatic C=N stretching at 1650 cm^{-1}). The principle absorption peaks of Flu are observed in the spectrum in the composite material (SBA15-Flu, green line), indicating that no covalent interactions between the components had occurred, that is, the dispersion of the Flu in the porous matrix does not change the primitive structure.

Figures 5 a exhibits the ^{29}Si magic angle spinning nuclear magnetic resonance (MASNMR) spectra for a) the SBA15 matrix as synthesized and b) SBA15 after heat treatment at 550 °C. The blue line shows three signals at 111.9, 101.8, and 93.2 ppm, which correspond to: Q_2 $(SiO)_2Si(OH)_2$, Q_3 $(SiO)_3Si(OH)$, and Q_4 $(SiO)_4Si$ silicon atom environments, respectively.[50]

After calcination of the synthesized SBA15 sample, the Q_2/Q_3 and Q_3/Q_4 ratios decrease, owing to the condensation of the silanol groups and the silicon network shrinkage.

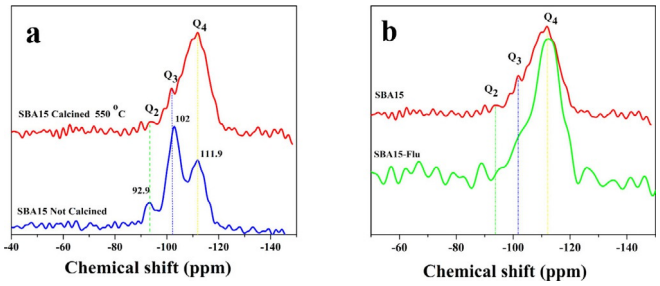

Figure 5. ^{29}Si NMR spectra of SBA15 a) before and after heat treatment at 550 °C and b) before and after the adsorption of Flu (SBA15-Flu).

In the case of the of composite material (SBA15-Flu) sample, the ^{29}Si NMR spectrum schematized in Figure 5b shows a decrease in the Q_2 and Q_3 signals, as compared to the ^{29}Si NMR spectrum of SBA15 calcined at 550 °C. This indicates that Flu adsorption occurs mainly through hydrogen bonding with silanol groups.

Figures 6a–6c show TGA/DSC analysis results. The initial 3.3% Flu sample mass loss in Figure 6a between 35 and 125 °C corresponds to the removal of the extraction solvent; the second mass loss (1.04%), before Flu fusion begins, occurs between 125 and 242 °C, and can be attributed to total desolvation;[51] at 242 °C, the crystallization of the compound begins, which melts and disintegrates at 375 °C. After that, the final weight loss is attributed to residues of the Flu precursors.[52] The DSC curve for Flu in the same figure displayed an endothermic band (desolvation) at 90 °C; the process also presents two exothermic peaks at temperatures that correlate with the decomposition of Flu and the organic residues. Figure 6b depicts the TGA/DSC of the SBA15 sample. Although the total loss of material during the process was 10.6%, consistent with the results of Ramanjaneya and Chennakesavulu,[53] the TGA line reveals three weight losses at temperatures of 35–200, 200–500, and 500–900 °C. The first is attributed to the dihydroxylation of the silicon matrix, the second is mainly due to residual degradation of organosilanes, and the final one occurs when the minimal weight loss takes place, that is, the porous structure of the matrix collapses and a significant part of its specific surface area is lost.[54] This analysis demonstrates the thermal stability of the SBA15-type materials. The DSC spectrum indicates an endothermic process.[55]

The thermal degradation of SBA15-Flu is presented in Figure 6c. As expected, the weight loss around 400 °C corresponds to 26.34% of the total weight of the sample, which is consistent with the Flu amount in the composite material (SBA15/Flu = 3:1 weight ratio). A second weight loss between 405 and 597 °C, of approximately 10.6%, was attributed to the decomposition of the organosilanes in the porous matrix of SBA15. Finally, the minimal mass loss above 600 °C is attributed to the disintegration of internal silanol groups (bound water);[56] this is the cause of the collapse of the structure of the material. The heat flow (red line) spectrum of SBA15-Flu shows two endothermic and two exothermic events; the first two correlate with the fusion and decomposition of Flu and the last two are from the same degradation processes of the SBA15 matrix.

2.2. Electrochemical Tests

When a medium has the necessary characteristics to trigger the corrosion process, the exposure time only alters the quantities of elements present in the metal corrosion products.[57] If iron is submerged into electrolytic solution containing Cl^-, the metal corrodes locally (pitting corrosion), owing to the chloride ions replacement of oxygen ions in the oxide lattice (corrosion products film) allowing the formation of chloride complexes with the metal cations; this situation is faster in the presence of sulfate ions (depending upon its ratio).[58,59] In this work, an environment with a ratio Cl^-/SO_4^{2-} of 7 was simulated.

Authors as Murray and Hack,[60] Grandle and Taylor,[61] and Akbarinezhad and Faridi[62] stated that the most useful parameter to evaluate the performance of a coating is the value of maximum impedance at low frequencies. This value is obtained from the $|Z|$ versus frequency plots. Taking this into consideration, Figure 7 shows the Bode plots for Z_{mod} and the corresponding phase angle diagrams (Figures 7a and 7b, respectively) for the EIS test made on the mild steel substrates covered with an NR coating (without SBA15-Flu composite) immersed in the electrolytic solution. From Figure 7a, the $|Z|_{0.01\,Hz}$ value, 10 min after immersion (time = 0) was 5.9 GΩ cm^2, showing the barrier properties of the NR coating. This value decreases over time (3×10^6 Ω cm^2 h^{-1}) as a consequence of the coating degradation, owing to the aggressive ion penetration, which reaches the metal-coating interface and initiates the metal corrosion process. The trend in the behavior of the phase angle plots over time, mainly in the intermediate frequencies range (Figure 7b), shows the transition from a purely capacitive behavior to a resistive response of the system.

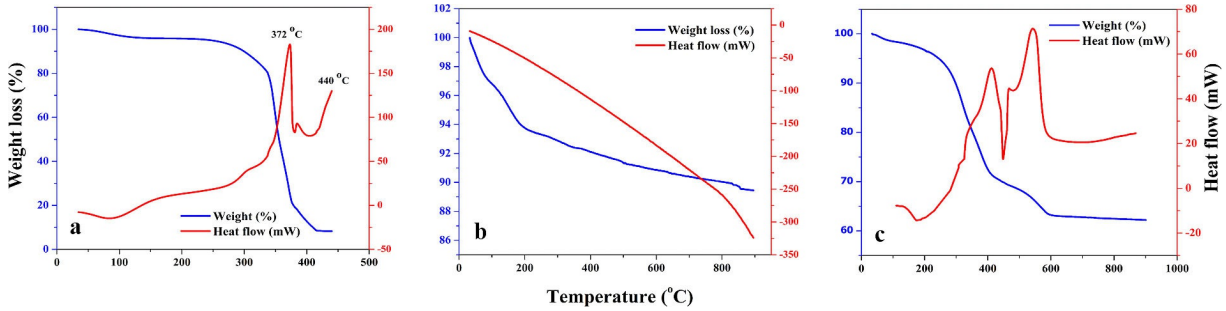

Figure 6. TGA/DCS spectra of a) Flu, b) the SBA15 porous matrix, and c) the composite material (SBA15-Flu).

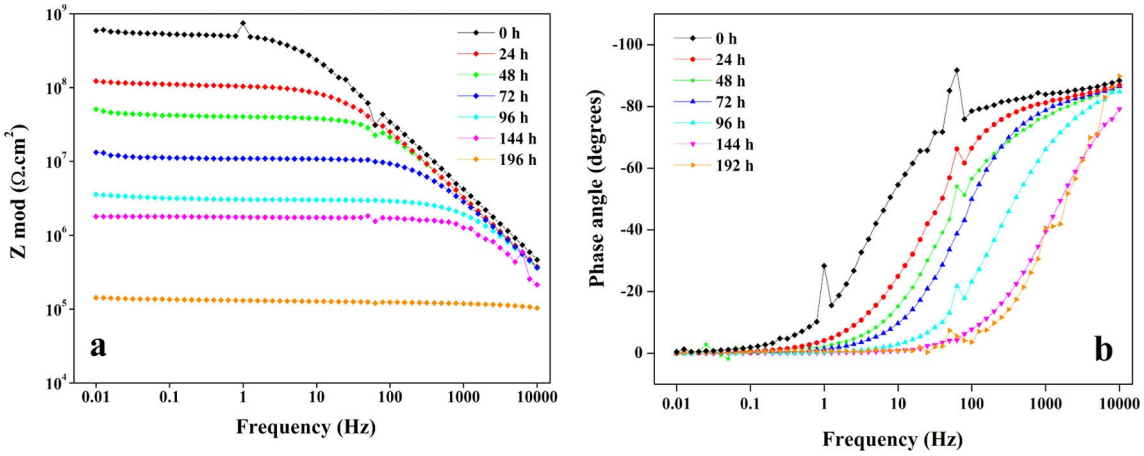

Figure 7. a) Z_{mod} versus frequency and b) phase angle versus frequency Bode plots for a mild steel substrate covered with a coating formulated without SBA15-Flu immersed in an electrolytic solution of pH 6.4.

The plots in Figure 8 and Figure 9 depict the EIS Bode plots for the mild steel substrates coated with the NR/SBA15-Flu film; one of them was scratched after 48 h of immersion (Figure 9) to evaluate the self-healing property of the coatings. These results show excellent protection against the corrosion process. The $|Z|$ versus frequency plots (Figure 8a) present a $|Z|_{0.01\,Hz}$ value at the beginning of the immersion of 3.2 GΩ cm^2, which decreased over time to a total impedance $|Z|_{0.01\,Hz}$ value of 3.7×10^7 GΩ cm^2, that is, with a ratio of 1.6×10^7 Ω cm^2 h^{-1}. This measure is in contrast with the impedance values obtained with the NR system (in Figure 7), which presented a two orders of magnitude reduction at the end of the immersion time. Figure 8b depicts the corresponding angle phase plots. The results in Figure 9a and Figure 9b correspond to the electrochemical evaluation for the NR/SBA15-Flu system scratched after 48 h of immersion. Again, according to the $|Z|_{0.01\,Hz}$ value, the trend of the coating degradation and the increase in the corrosion conditions caused by the penetration of the aggressive ions are observed. The effect of the activity of the inhibitor is reflected in the EIS evaluation immediately after the scratching the surface. The $|Z|_{0.01\,Hz}$ response (1350 Ω cm^2) corresponds to a surface that is not covered. However, over time, that is, after 192 h of immersion, the $|Z|_{0.01\,Hz}$ system reaches a value of 2.4×10^5 Ω cm^2, similar to the response of the surface covered with NR. This behavior can be attributed to the release of the inhibitor from the porous matrix at the moment that it interacts with the electrolyte. As the corrosion inhibition mechanism of an organic inhibitor (comprising π electrons, double conjugated bonds, and heteroatoms such as nitrogen) corresponds to the formation of a metal surface protective film, it originates from coordinated bonds with outer and empty iron orbital (or metal) atoms.[63,64]

Figure 10 presents $|Z|_{0.01\,Hz}$ as a function of time for the evaluated systems (both the scratched and unscratched coatings, as well as those corresponding to the metal without a coating). The red line indicates an abrupt impedance decrease at the scratching time of the coating. After that, the system subsequently recovered the film, that id, the $|Z|_{0.01\,Hz}$ value increased with the time, reaching 2.5×10^5 GΩ cm^2, with a ratio of 1.7×10^4 Ω cm^2 h^{-1}; this could be attributed to the inhibitor protective behavior, which was released from the porous matrix as soon as it contacted the electrolytic solution. The

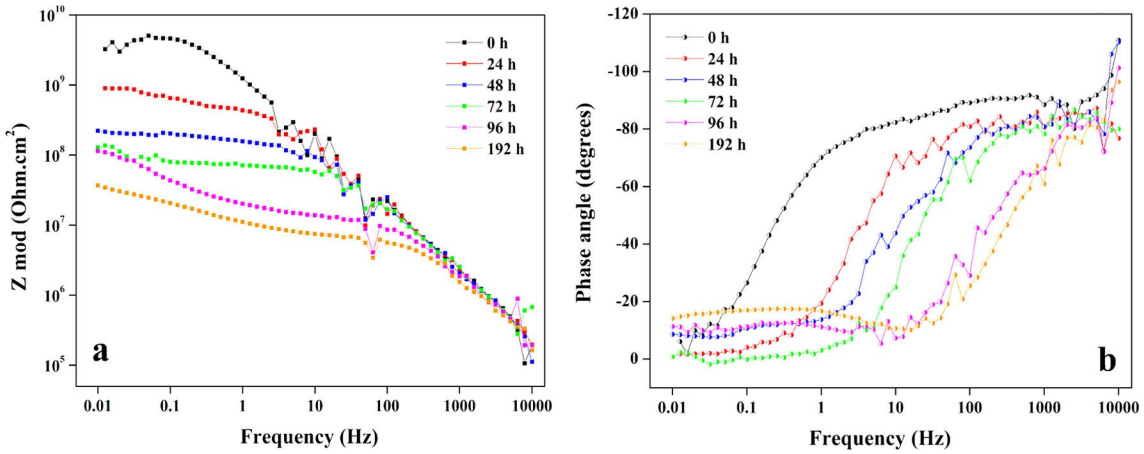

Figure 8. a) Z_{mod} versus frequency and b) phase angle versus frequency Bode plot for a mild steel substrate covered with a coating formulated with SBA15-Flu immersed in an electrolytic solution at pH 6.4.

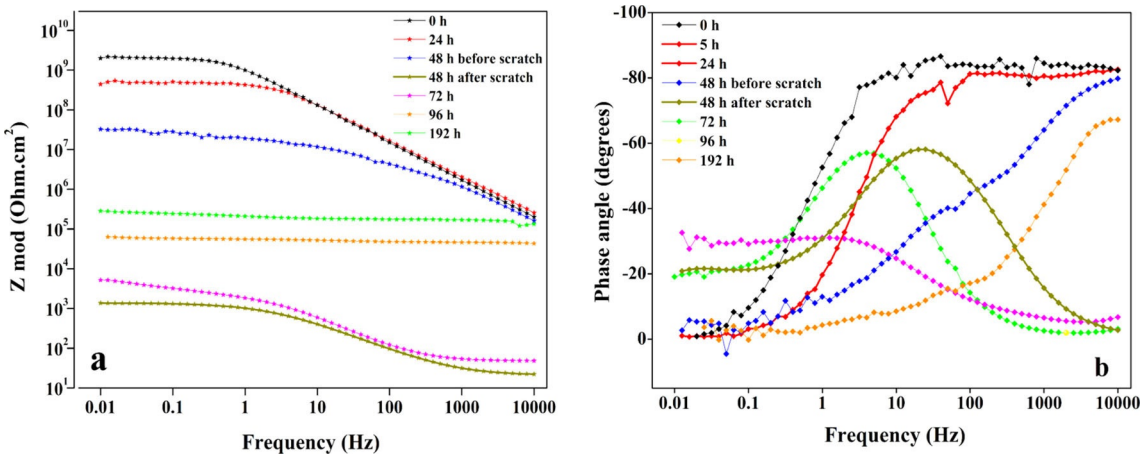

Figure 9. a) Z_{mod} versus frequency and b) phase angle versus frequency Bode plot for a mild steel substrate covered with a coating formulated without SBA15-Flu scratched after 48 h after the immersion in an electrolytic solution at pH 6.4.

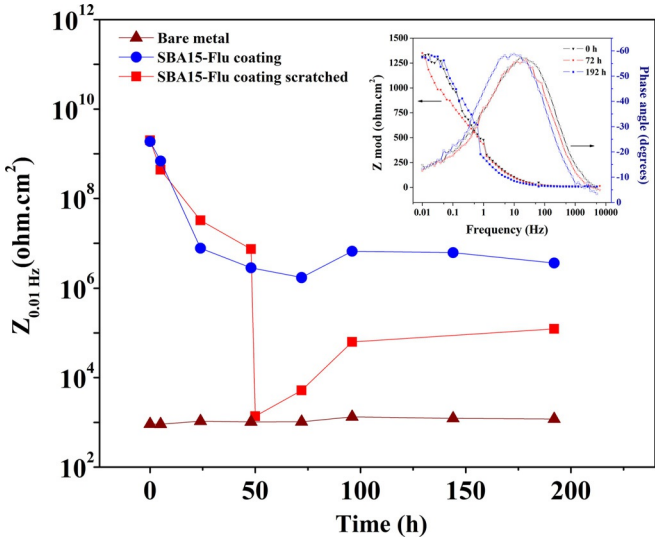

Figure 10. $|Z|_{0.01\,Hz}$ of the systems immersed in electrolytic solution prepared with NaCl and $(NH_4)_2SO_4$; inset: Bode plots of the bare mild steel. The open circuit potential (OCP) over time for the different systems can be seen in Figure S2 of the Supporting Information.

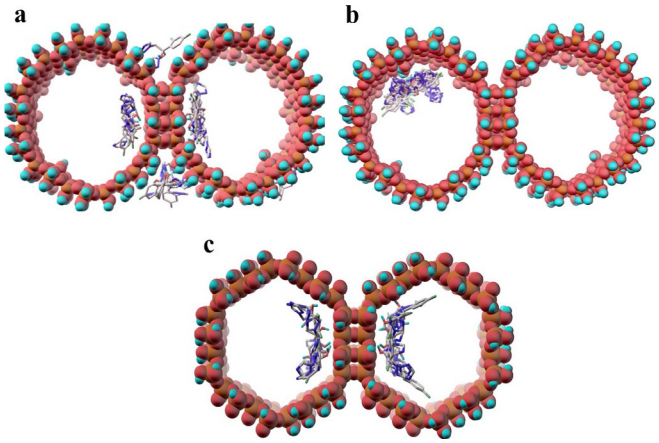

Figure 11. Highest scoring configurations of Flu with SBA15 obtained by docking simulations using the AutodockVina program:[86,89] a) on the surface of SBA15 with Flu (SF1), the most favorable site is indicated with an arrow; b) interaction inside the pores of SBA15 with Flu (SF2); and c) on SBA15 with Flu (SF3). The 20 most favorable poses of 100 for each case were considered.

inset shows the bare metal Bode plots only for comparative purposes; the $|Z|_{0.01\,Hz}$ values obtained are given in Figure 10 (wine-colored line).

2.3. Computational Docking for the SBA15-Flu Composite

Docking simulations were used to model the interactions between SBA15 and Flu, as well as for their characterization. The binding energies obtained by docking analyses were from −20.1 to −15.5 kJ mol^{-1}. Figure 11 a depicts the highest scoring conformers of Flu on the surface of SBA15 considering internal hydroxyl groups (SF1), whereas Figure 11 b shows the interaction of Flu with hydroxyl groups inside the pores of SBA15 (SF2). Figure 11 c shows Flu with the highest scoring interaction with SBA15 hydroxylated-free (SF3).

Binding free energy (ΔG_b) calculations. Altogether, these models allowed us to determine the polar (ΔG_p) and nonpolar (ΔG_{np}) contributions to ΔG_b in the SBA15-Flu interaction for the highest scoring configurations. The more favorable configuration for each case is shown in Table 2, where the $\Delta G_b < 0$ for SBA15 with Flu is evident. For the SF2 systems ($\Delta G_b =$ −1073 kJ mol^{-1}) and SF3 ($\Delta G_b = -506.6$ kJ mol^{-1}), the results in-

Table 2. Binding energy (ΔG_b) for the SBA15-Flu system determined by APBS[59] and VMD 1.9.1.[60]

Composite	$\Delta G_{solvatation}$ [kJ mol^{-1}]	$\Delta G_{coulombic}$ [kJ mol^{-1}]	ΔG_{np} [kJ mol^{-1}]	ΔG_b[a] [kJ mol^{-1}]
SF1 (Figure 11 a)	2.3	1.0	−8.3	−4.9
SF2 (Figure 11 b)	8.4	−1079	−2.7	−1073
SF3 (Figure 11 c)	8.2	−507	−7.8	−506.6

[a] $\Delta G_b = \Delta G_p + \Delta G_{np}$, where $\Delta G_p = \Delta G_{solvatation} + \Delta G_{coulombic}$.

dicate that polar interactions drive the binding mostly by the coulombic contribution rather than by nonpolar interaction; however, for SF1, the binding is governed mainly by nonpolar interactions and, in a minor proportion, by polar interactions ($\Delta G_b = -4.9$ kJ mol^{-1}). Four binding sites for SF1 were found; the most favorable is indicated with an arrow in Figure 11a; the rest of the configurations displayed in the other sites presented a ΔG_b value < -1.9 kJ mol^{-1}, indicating that the polar interactions were unfavorable.

The above results may be related to the way that Flu molecules are released; the smaller the binding energy is, the shorter the time it takes to be released and vice versa. Therefore, understanding the molecular interactions responsible for the controlled release mechanism of the Flu molecules in this composite is essential. The next section is intended to grasp the principles underlying this process by means of quantum chemical simulations.

2.4. Electron Density Analysis

Figures 12a–12c show molecular graphs of the SF1, SF2, and SF3 clusters, respectively, obtained with QTAIM. The orange tubes between Flu and the clusters represent the intermolecular interactions between Flu and SBA15. These interactions were classified into two groups: F···O, O···O, N····O, and C···O, belonging to non-canonical weak interactions; and O–H···O, O–H···N, and O–H···F, categorized as hydrogen bonds. Although it is not clear that the four contacts of the former group could be in the bond categories of halogen, chalcogen, pnicogen, or tetrel,[65–73] which have been explained mainly in electrostatic terms because of the presence of sigma holes,[74] it is recognized that these contribute to the stability of molecular clusters and crystals and, therefore, must have an attractive nature. C–H···O can be considered a hydrogen bond,[72] albeit a weaker and non-classical type.[75] For both groups of interactions, low values of the electron density were searched, with the Laplacian (positive in each case) and the virial field at the bond critical points (BCPs). This is characteristic of non-covalent interactions.

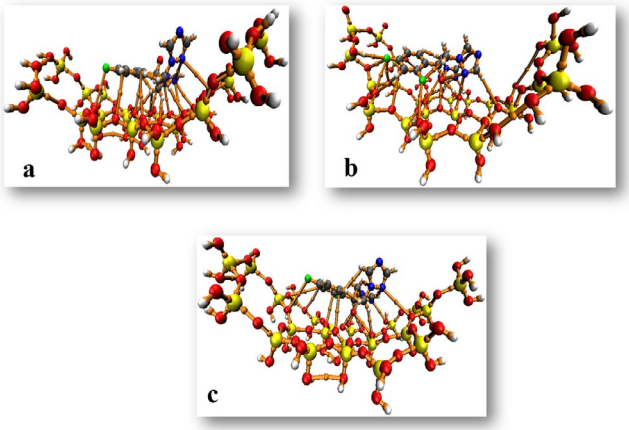

Figure 12. Molecular graphs of a) SF1, b) SF2, and c) SF3.

Figure 13 presents histograms of the different atomic contacts. The distribution is dependent on the orientation of the Flu molecule, as well as of the presence of a hydroxyl group close to Flu; the latter condition being fulfilled solely in SF2 (Figure 12b). It is interesting to note that both cases, a bond path linking the Flu molecule with Si atoms is not found. The only contacts detected in each of the clusters are the F···O, N···O, and C–H···O. Owing to the reason mentioned above, the strong hydrogen bonds manifested only on the SF2 complex (Figure 12b). As expected from the ΔG_b analysis (see Table 2), this structure has more contacts than SF1 (Figure 12a) and SF3 (Figure 12c).

Nonetheless, their contribution to the net stability of the cluster is more important than the number of contacts. With this purpose in mind, the electron density evaluated at the bond critical points (ρ_{BCP}), was used as a general criterion for the strength of each kind of interaction. Figure 14 shows the graph of ρ_{BCP} as a function of the distance (R) between every pair of connected atoms. Large values of ρ_{BCP} and short distances imply stronger interactions. It is noticed that SF1 (Figure 14a) has the weaker interactions, in agreement with Table 2. As expected, the hydrogen bonds, particularly the O–H···H interaction that appears at the shortest distance of 1.994 Å, provide important stability in all of the clusters, especially for SF2 (Figure 14b). This outcome explains why SF2 (Figure 14b) has the more negative ΔG value with a strong electrostatic component, as classical hydrogen bonds tend to display this behavior. Consistently, within the approach of Espinosa et al.,[76] where the interaction energy of a hydrogen bond is related to the potential energy density at the BCP by a factor of 0.5, these types of interactions contribute -20.09, -48.14, and -7.95 kJ mol^{-1} to the SBA15-Flu interaction in SF1 (Figure 14a), SF2 (Figure 14b) and SF3 (Figure 14c), respectively. An abnormally large value of ρ_{BCP} is observed in SF3 (Figure 14c) for an O···O contact. This result is possibly a consequence of the closeness between the two oxygen atoms, as the interatomic distance is almost 0.7 Å shorter than the sum of the van der Waals radii, and do not necessarily involve a strong interaction.

Finally, from the NCI isosurfaces (Figure 15), it was inferred that the non-canonic interactions of the first group have a dispersive origin, as can be seen in the flat green isosurfaces. The green disk of the non-classical C–H···O contacts confirms its weak hydrogen-bond nature. The blue isosurfaces associated with the O–H···X (X = O, N or F) contacts corroborate the strong electrostatic nature of these interactions. An unusual yellow-reddish surface around each Si atom is observed, which could be related to the tension of the Si–O–Si angles (ca. 150°), which deviate considerably from the ideal value for sp^3 hybridization.

3. Conclusions

The results of the characterization showed the integrity of the inhibitor molecule in the composite material. Nitrogen adsorption analysis confirmed the ability of the nanoporous matrix as a vehicle for the retention and subsequent release of the cor-

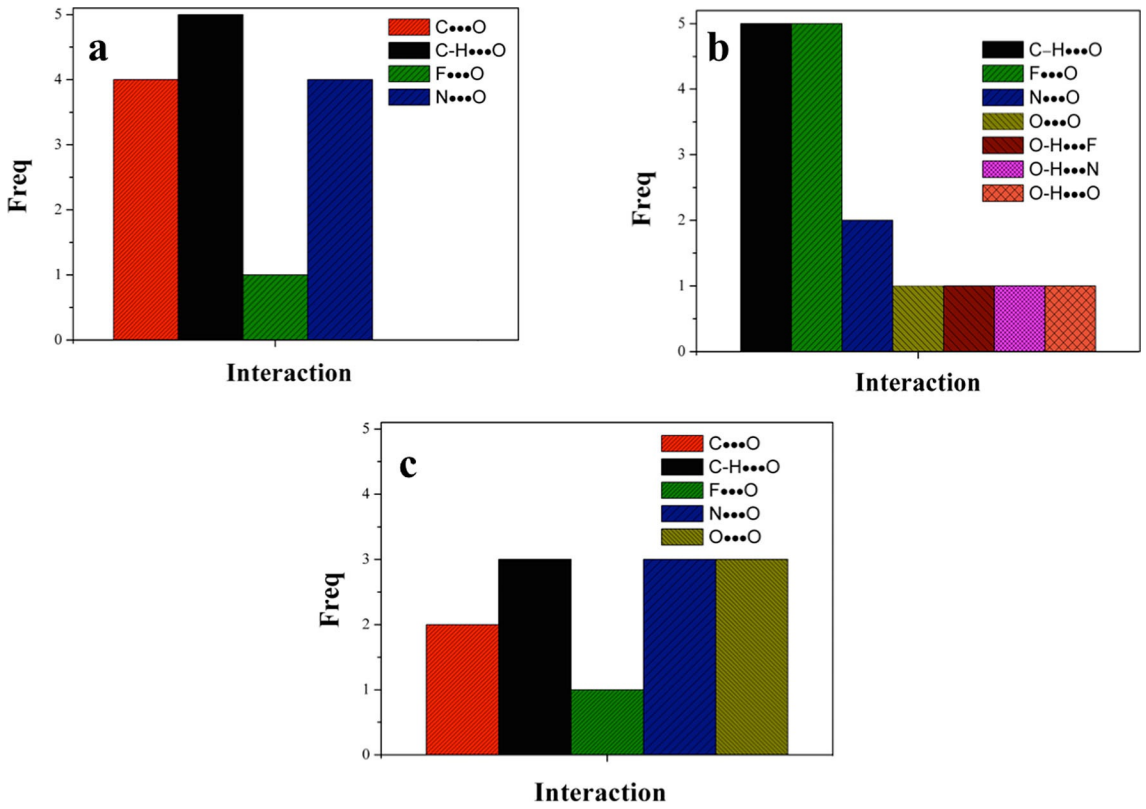

Figure 13. Histograms of the different interactions manifested in a) SF1, b) SF2, and c) SF3.

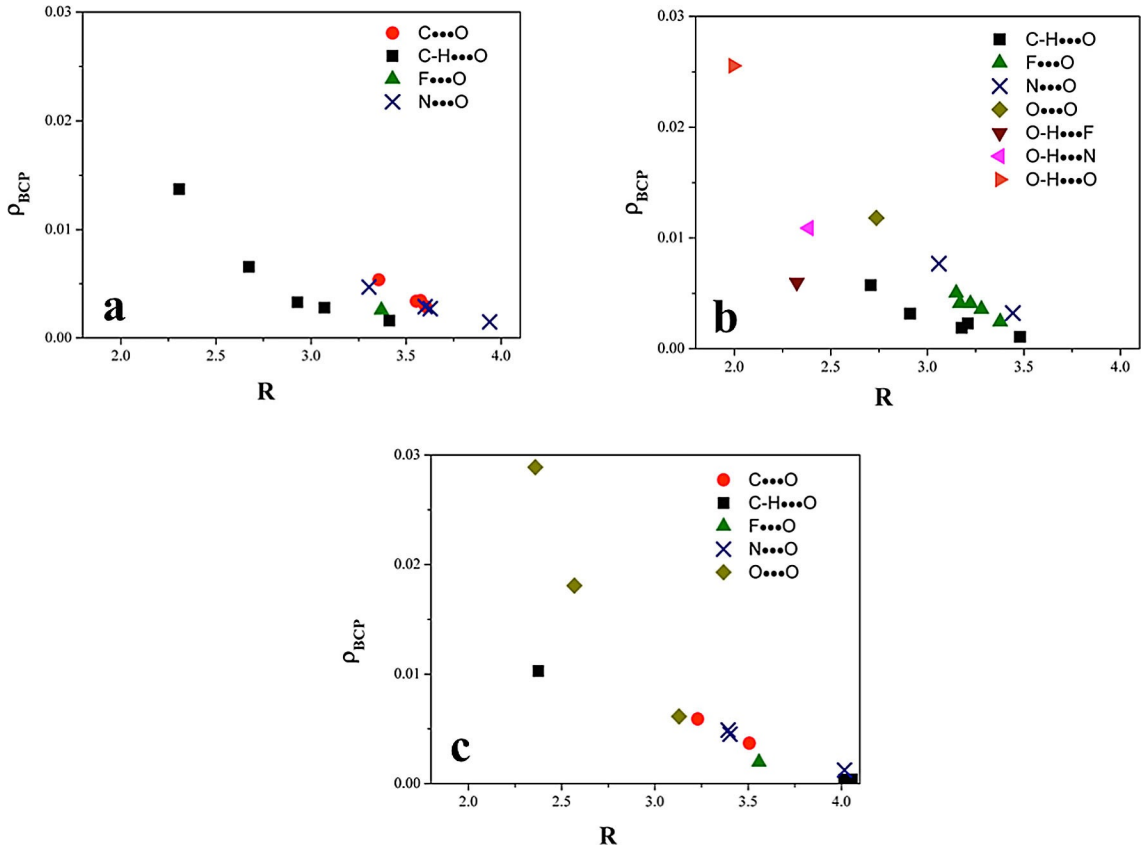

Figure 14. ρ_{BCP} as a function of the distance (R) between the atoms connected by bond paths for a) SF1, b) SF2 and c) SF3. ρ_{BCP} and R units are given in a.u. and Å, respectively.

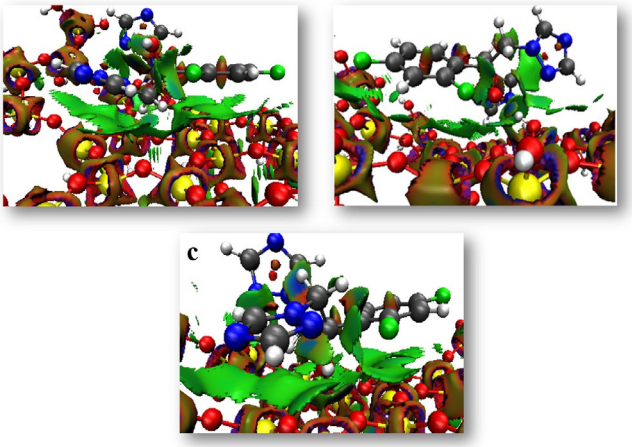

Figure 15. NCI isosurfaces of a) SF1, b) SF2, and c) SF3 drawn at 0.7 a.u.

rosion inhibitor (fluconazole molecules). EIS evaluation indicates that the entrapped Flu molecules could be released from the porous matrix, providing the protective coating with the "self-healing" characteristic. Differences in binding energies could explain the mechanism of controlled release of the corrosion inhibitor dispersed in the matrix, that is, the smaller the binding energy is, the shorter the time it takes to be released and vice versa. The electron density analysis provides information about the microscopic nature of the intermolecular interactions responsible for the adsorption processes in the different binding sites. The three classes of systems characterized in this study are stabilized by non-canonical interactions: F···O, O···O, N···O, C···O, as well as weak C–H···O hydrogen bonds. Nonetheless, strong O–H···O, O–H···N, and O–H···F hydrogen bonds were identified only on SF2, which in turn help to explain why it has a larger ΔG_b value with a substantial electrostatic contribution. In contrast, SF1 and SF3 complexation have mainly a dispersive origin.

Experimental Section

Synthesis of Mesoporous Matrix (SBA15).

To synthesize the SBA15 material, the sol-gel technique developed by Zhao et al.,[77] was used, together with the method conditions reported by Esparza et al.,[78] using 4 g of Pluronic 123 dissolved in a 2 M HCl solution as a structure director. Afterwards, 4 mL of tetraethyl-orthosilicate (TEOS) was added to the acid solution as a source of silicon, drop by drop under vigorous stirring for 1 h. Then, the reaction was aged at 50 °C for approximately 24 h, and the obtained sol was placed in a heating mantle at 80 °C for a further 48 h. The white gel obtained was filtered and first washed with abundant distilled water, and finally with anhydrous ethyl alcohol. The precipitate wass dried and subjected to heat treatment at 550 °C.

Fluconazole Extraction

Flu was obtained from expired pharmaceuticals[79] by dissolving a capsule of the drug in 20 mL of methanol and subsequently evaporating the solvent.

Composite Material Preparation (SBA15 Particles Loaded with Flu Inhibitor)

The SBA15 porous matrix was dispersed in a methanol solution containing the Flu particles. Four SBA15-Flu composites were prepared with different weight ratios of 6:1, 3:1, 2:1, and 1:1 in order to observe the entrapped Flu molecules in the porous matrix.

Coating Preparation

The SBA15-Flu composite with a 3:1 ratio (3% wt) was dispersed in a nitrocellulose resin. To ensure the homogeneity of the mixture, the formulation was sonicated for approximately 10 min at 42 kHz frequency and 70 °C.

Characterization Techniques

The surface morphology was obtained by using a Jeol 2100F high-resolution transmission electron microscope and an Oxford model INCA energy-dispersive X-ray detector. Nitrogen adsorption studies were carried out in a Micromeritics ASAP 2020 device at 77 K. FTIR spectra were obtained on a Bruker ALPHA instrument. XRD studies were carried out on a Bruker D8-PHASER diffractometer. Solid-state ^{29}Si HPDEC NMR spectra were recorded at 59.62 MHz with a Bruker Avance-II 300 spectrometer, and a PerkinElmer diamond TGA/DSC thermogravimetric differential thermal analyzer was used to evaluate the thermal decomposition with a heating speed of 20 °C min^{-1} under an N_2 flow rate of 50 mL min^{-1}.

To evaluate the protective behavior of the system, EIS was used. The mild steel substrates were covered with the synthesized coatings, achieving a film thickness of 16(+/−4) μm. The corrosion tests were accomplished by immersing the working electrode in an electrolytic solution prepared with 26.5 g of sodium chloride and 3.8 g of ammonium sulfate, meaning that the Cl^-/SO_4^{2-} ratio was 7. The impedance Bode plots were recorded by using a typical three-electrode cell (Ag/AgCl as a reference electrode, a graphite bar as a counter electrode, and the working electrode) connected to a Gamry Instruments potentiostat/galvanostat. The amplitude sinusoidal potential was15 mV through a sweep of frequencies from 0.01 to 10000 Hz.

Computational Studies: SBA15 and Flu Structures

We used the MCM-41 layer model[42,80] to represent the SBA15 model. The addition of internal hydroxyls to our SBA15 model (SF1 and SF2) was performed according to the results described by Vasant et al.,[81] in which hydroxyl groups are measured as a function of the temperature of the SiO_2 material, considering the calcination temperature of our SBA15 material (550 °C). Hydroxylate-free SBA15 was also modeled (SF3). Three conformers of the Flu molecule were taken from X-ray data of different polymorphs.[82,83] For each structure, two conformational analyses were applied to get low-energy arrangements: a) a systematic search over 500 000 conformers with the AMMP package through the VEGA ZZ suite,[84] using the SP4 force field;[85] and b) a genetic algorithm search over 100 conformers with the Avogadro Software[86] and the Universal Force Field.[87] Next, geometry optimizations were carried out over both the initial and the found conformers at a B3LYP-D3(BJ)/def2-TZVP level of theory with the NWChem software package.[88] For the docking analysis, we selected the six conformers with the lowest energy from the optimized structures (see Figure S1 of the Supporting Information).

Computational Docking: Interactions between SBA15 and Flu Molecules

SBA15 models were prepared, as described above, and employed for docking assays with Flu. They were performed by using the AutodockVina program[57] requiring 100 configurations for SF1, SF2, and SF3. For detailed analysis of the interactions at a binding site, the configurations with the best binding energy values in each case were chosen.

Binding Energy

We followed the same protocol as in our previous reports.[89–92] The dielectric constants were 78 and 2 for water and SBA15,[93] respectively. The atomic charges for SBA15 and Flu were chosen from the force field implemented in the AutodockVina program.[94] The binding energies for the best configurations are shown in Table 2 and were determined with Adaptive Poisson–Boltzmann Solver program (APBS)[95] for polar contributions, and with the program Visual Molecular Dynamics 1.9.1 (VMD 1.9.1) for nonpolar contributions.[96]

QTAIM and NCI Analysis

For the simulation of the SBA15-Flu interactions, three clusters were built from the most stable complexes of the docking analysis. A cut-off distance of 7 Å from the Flu molecule was taken to construct these clusters and reduce the size of the system under study. Hydrogen atoms were added to saturate the terminal oxygen atoms. The first two SBA15-Flu clusters (SF1 and SF2) were modeled from the most stable SBA15-Flu structures containing internal hydroxyls, whereas the third (SF3) came from the most stable hydroxylated-free complexes. Nonetheless, no hydroxyls were found nearby the Flu molecule in SF1. Single-point energy calculations over the three clusters at the B3LYP/def2-TZVP level of theory with NWChem code was performed. Determination of the BCPs as well as the NCI isosurface computations were carried out with the GPUAM software.[97]

Acknowledgements

The authors thank the Project No. 12413235/917073 from PRODEP-SEP and Ing. Patricia Castillo for technical support with the TEM. We are also grateful to the Laboratorio de Supercómputo y Visualización en Paralelo at the Universidad Autónoma Metropolitana (UAM) Iztapalapa for access to their computer facilities. B. L.-R. thanks UAM for a postdoctoral fellowship.

Conflict of Interest

The authors declare no conflict of interest.

Keywords: docking studies · Fluconazole · quantum theory of atoms in molecules · self-healing coatings · SBA15

[1] L. Barchi, U. Bardi, S. Capoali, M. Fantini, A. Scrivani, *Prog. Org. Coat.* **2010**, *67*, 146 – 151.
[2] D. Pradham, R. G. Reddy, *Mater. Chem. Phys.* **2014**, *143 – 2*, 564 – 569.
[3] K. Uehara, K. Yamazaki, T. Gunji, S. Kaneko, T. Tanabe, T. Ohsaka, F. Matsumoto, *Electrochim. Acta* **2016**, *215 – 10*, 556 – 565.
[4] S. A. Khan, Y. Miyashita, Y. Mutoh, *Mater. Corros.* **2015**, *66*, 940 – 948.
[5] P. Jehl, B. Halbedel, M. Lerp, U. Chimidt, G. Teichert, F. Chlutter, *Key Eng. Mater.* **2017**, *742*, 434 – 439.
[6] A. Stankiewicz, I. Szczygiel, B. Szczygiel, *J. Mater. Sci.* **2013**, *48*, 8041 – 8051.
[7] J. Liu, Y. Zhang, S. Li, B. Xue, X. Yin, *Prog. Org. Coat.* **2015**, *81*, 93 – 100.
[8] M. Zhou, L. Yan, H. Ling, Y. Diao, X. Pang, Y. Wang, K. Gao, *Appl. Surf. Sci.* **2017**, *404*, 246 – 253.
[9] L. C. Vosgien, D. Trinh, G. Bouvet, X. Feaugas, S. Mallarino, S. Touzain, *Electrochim. Acta* **2017**, *234*, 7 – 15.
[10] J. M. Falcon, L. M. Otubo, I. V. Aoki, *Surf. Coat. Technol.* **2016**, *303*, 319 – 329.
[11] E. Shchukina, D. Shchukin, D. Grigoriev, *Prog. Org. Coat.* **2017**, *102*, 60 – 65.
[12] A. Keyvani, M. Yeganeh, H. Rezaeyan, *Prog. Nat. Sci.* **2017**, *27*, 261 – 267.
[13] S. R. White, N. R. Sottos, P. H. Geubelle, J. S. Moore, S. R. Kessler, E. N. Brown, S. Viswanathan, *Nature* **2001**, *409*, 794 – 797.
[14] D. V. Andreva, D. G. Shchukin, *Mater. Today* **2008**, *11*, 24 – 30.
[15] D. G. Shchukin, H. Möhwald, *Adv. Funct. Mater.* **2007**, *17*, 1451 – 1458.
[16] E. Abdullayev, R. Price, D. Shchukin, Y. Lvov, *ACS Appl. Mater. Interfaces* **2009**, *1*, 1437 – 1443.
[17] E. V. Skorb, D. G. Shchukin, H. Möhwald, D. V. Sviridov, *J. Mater. Chem.* **2009**, *19*, 4931 – 4937.
[18] G. L. Li, Z. Zheng, H. Möhwald, D. G. Shchukin, *ACS Nano* **2013**, *7*, 2470 – 2478.
[19] D. Snihirova, S. V. Lamake, M. Taryba, A. M. Salak, S. Kallip, M. L. Zheludkevich, M. G. S. Ferreira, M. F. Montemor, *ACS Appl. Mater. Interfaces* **2010**, *2*, 3011 – 3022.
[20] M. F. Montemor, D. V. Snihirova, M. G. Taryba, S. V. Lamaka, I. A. Kartsonakis, A. C. Balaskas, G. C. Kordas, J. Tedim, A. Kuznetsova, M. L. Zheludkevich, M. G. M. Ferreira, *Electrochim. Acta* **2012**, *60*, 31 – 40.
[21] M. Plawecka, D. Snihirova, B. Martins, K. Szczepanowicz, M. F. Warszynki, M. F. Montemor, *Electrochim. Acta* **2014**, *140*, 282 – 293.
[22] J. Falcón, T. Sawczen, A. Vieira, *Frontiers in Materials* **2015**, *2*, 1 – 13.
[23] Y. C. Feng, Y. F. Cheng, *Corros. Eng. Sci. Technol.* **2016**, *51*, 489 – 497.
[24] Y. He, W. Xu, R. Tang, CH. Zhang, Q. Yang, *RSC Adv.* **2015**, *5*, 90609 – 90620.
[25] S. M. Lópes dos Santos, K. A. Barros Nogueira, M. De Souza Gama, J. D. Ferreira, I. J. Da Silva Júnior, D. C. Silva de Azevedo, *Microporous Mesoporous Mater.* **2013**, *180*, 284 – 292.
[26] Q. Li, H. Yu, J. Song, X. Pan, J. Liu, Y. Wang, L. Tang, *Appl. Surf. Sci.* **2014**, *290*, 260 – 266.
[27] F. Azimov, I. Markova, V. Stefanova, K. Sharipov, *J. Univ. Chem. Tech. Metallurgy* **2012**, *47*, 333 – 340.
[28] L. Liang, Z. Zheng, H. Mohwamald, D. G. Shchukin, *ACS Nano* **2013**, *7*, 2470 – 2478.
[29] V. Bustos-Terrones, J. Uruchurtu, J. J. Rochín-Medina, K. Ramírez, J. G. Rangel-Peraza, M. Romero-Romo, Y. Bustos-Terrones, *Surf. Eng.* **2018** https://doi.org/10.1080/02670844.2018.1507510.
[30] A. L. Doadrio, E. M. B. Sousa, J. C. Doadrio, J. Pérez-Pariente, I. Izquierdo-Barba, M. Vallet-Regí, *J. Controlled Release* **2004**, *97*, 125 – 132.
[31] M. Manzano, M. Vallet-Regí, *J. Mater. Chem.* **2010**, *20*, 5593 – 5604.
[32] D. Halamová, M. Badanicová, V. Zelenák, T. Gondová, U. Vainio, *Appl. Surf. Sci.* **2010**, *256*, 6489 – 6494.
[33] T. Limmell, T. Heikkila, H. A. Santos, S. Sistonen, S. Hellsten, T. Laaksonen, L. Peltonen, N. Kumar, D. Y. Murzin, M. Louhi-Kultanen, J. Salonen, J. Hirvonen, V. P. Letho, *Int. J. Pharm.* **2011**, *416*, 242 – 251.
[34] V. Ambrogi, L. Periolo, C. Pagano, F. Marmottini, M. Ricci, A. Sagnella, C. Rossi, *Eur. J. Pharm. Sci.* **2012**, *46*, 43 – 48.
[35] A. Kiwilsza, B. Milanowski, K. Druzbicki, L. Emerson, M. Grzeszkowiak, M. Jarek, J. Mielcarek, J. Lulek, A. Pajzderska, J. Wasicki, *J. Porous. Mater.* **2015**, *22*, 817 – 829.
[36] S. K. Natarajan, S. Selvaraj, *RSC Adv.* **2014**, *4*, 14328 – 14334.
[37] I. Izquierdo-Barba, E. Sousa, J. C. Doadrio, A. L. Doadrio, J. Pérez-Pariente, A. Martínez, F. Babonneau, M. Vallet-Regí, *J. Sol-Gel Sci. Technol.* **2009**, *50*, 421 – 429.
[38] Q. Jin, F. Qu, J. Jiang, Y. Dong, W. Guo, H. Lin, *J. Sol-Gel Sci. Technol.* **2013**, *66*, 466 – 471.
[39] I. Jabbari, Z. Abadi, O. Sadeghi, H. Reza, L. Zhad, N. Tavassoli, V. Amani, M. Amini, *J. Sol-Gel Sci. Technol.* **2012**, *61*, 90 – 95.

[40] R. F. Popovice, E. M. Seftel, G. D. Mihai, E. Popovice, V. A. Voicu, *J. Pharm. Sci.* **2011**, *100*, 704 – 714.
[41] C. Ávila-González, R. Cruz-Silva, C. Menchaca, S. Sepúlveda-Guzman, J. Uruchurtu, *Nanotechnology* **2011**, *1 – 9*.
[42] C. T. Kresge, M. E. Leonowicz, W. J. Roth, J. C. Vartuli, J. S. Beck, *Nature* **1992**, *359*, 710 – 712.
[43] R. F. W. Bader, **1990**, *Atoms in molecules: a quantum theory.* Vol. 22, International series of monographs on chemistry.
[44] E. R. Johnson, S. Keinan, P. Mori-Sanchez, J. Contreras-Garcia, A. J. Cohen, W. Yang, *J. Am. Chem. Soc.* **2015**, *132*, 6498 – 6506.
[45] M. Thommes, K. Kaneko, A. V. Nimark, J. P. Oliver, F. Rodriguez-Reinoso, J. Rouquerol, K. S. W. Sing, *Pure Appl. Chem.* **2015**, *87*, 1052 – 1069.
[46] G. Z. Papageorgiou, D. Bikiaris, F. I. Kanaze, E. Karavas, A. Stergiou, *Drug Dev. Ind. Pharm.* **2008**, *34*, 336 – 346.
[47] R. M. Obaidat, K. A. Alkhamis, M. S. Salem, *Drug Dev. Ind. Pharm.* **2010**, *36*, 570 – 580.
[48] M. A. Smith, R. L. Lobo, *Microporous Mesoporous Mater.* **2010**, *131*, 204 – 209.
[49] H. Huang, Y. Ji, Z. Qiao, C. H. Zhao, J. He, H. Zhang, *J. Autom. Methods Manag. Chem.* **2010**, 323509.
[50] F. De Juan, E. Ruiz-Hitzky, *Adv. Mater.* **2000**, *12,* 430 – 432.
[51] K. A. Alkhamis, R. M. Obaidat, *Pharm. Dev. Technol.* **2002**, *7,* 491 – 503.
[52] J. Li, S. Zhang, Y. Zhou, S. Guan, L. Zhang, *J. Inclusion Phenom. Macrocyclic Chem.* **2016**, *84*, 209 – 217.
[53] R. G. Ramanjaneya, K. Chennakesavulu, *J. Mol. Struct.* **2014**, *1075*, 406 – 412.
[54] G. Chandrasekar, M. Hartmann, V. Murugesan, *J. Porous. Mater.* **2009**, *16*, 175 – 183.
[55] M. Bastianini, M. Sisani, A. Petracci, *Cosmetics* **2017**, *4*, 21.
[56] I. Díaz, F. Mohino, J. Pérez-Pariente, E. Sastre, *Thermochim. Acta* **2004**, *413*, 201 – 207.
[57] I. De la Fuente, I. Díaz, J. Simancas, B. Chico, M. Morcillo, *Corros. Sci.* **2011**, *5*, 604 – 617.
[58] R. R. Winston, H. Uhlig, **2008**. *Corrosion and corrosion control: an introduction to corrosion science and engineering, 4th Edition*, Wiley-Interscience, .
[59] P. Refait, J. M. R. Génin, *Corros. Sci.* **1994**, *36*, 55 – 65.
[60] J. N. Murray, H. P. Hack, *12th Int. Corros. Congr. Houston* **1993**, 151 – 155.
[61] J. A. Grandle, S. R. Taylor, *Corrosion* **1994**, *50*, 792 – 803.
[62] E. Akbarinezhad, H. R. Faridi, *Surf. Eng.* **2008**, *24*, 280 – 286.
[63] K. Hu, J. Zhuang, CH. Zheng, Z. Ma, L. Yan, H. Gu, X. Zeng, J. Ging, *J. Mol. Liq.* **2016**, *222*, 109 – 117.
[64] P. Kannan, R. T. Subba, N. Rajendran, *J. Mol. Liq.* **2016**, *222*, 586 – 595.
[65] A. Sirohiwal, V. R. Hathwar, D. Dey, R. Regunathan, D. Chopra, *Acta Crystallogr. Sect. B* **2017**, *73*, 140 – 152.
[66] A. M. Koohi, Z. Mahdavifar, S. Noorizadeh, *ChemistrySelect* **2017**, *2*, 2713 – 2717.
[67] D. J. Pascoe, K. B. Ling, S. L. Cockroft, *J. Am. Chem. Soc.* **2017**, *139*, 15160 – 15167.
[68] K. T. Mahmudov, M. N. Kopylovich, M. F. C. G. Da Silva, A. J. Pombeiro, *Dalton Trans.* **2017**, *46*, 10121 – 10138.
[69] S. Sarkar, M. S. Pavan, T. G. Row, *Phys. Chem. Chem. Phys.* **2015**, *17 – 4*, 2330 – 2334.
[70] A. Bauzá, T. J. Mooibroek, A. Frontera, *Angew. Chem. Int. Ed.* **2013**, *52*, 12317 – 12321; *Angew. Chem.* **2013**, *125*, 12543.
[71] A. Bauzá, T. J. Mooibroek, A. Frontera, *Chem. Rec.* **2016**, *16*, 473 – 487.
[72] G. Cavallo, P. Metrangolo, T. Pilati, G. Resnati, G. Terraneo, *Cryst. Growth Des.* **2014**, *14*, 2697 – 2702.
[73] A. J. Edwards, C. F. Mackenzie, P. R. Spackman, D. Jayatilaka, M. A. Spackman, *Faraday discuss.* **2017**, *203*, 93 – 112.
[74] J. S. Murray, P. Lane, P. Politzer, *J. Mol. Model.* **2009**, *15*, 723 – 729.
[75] G. R. Desiraju, *Acc. Chem. Res.* **1996**, *29*, 441 – 449.
[76] E. Espinosa, E. Molins, C. Lecomte, *Chem. Phys. Lett.* **1998**, *285*, 170 – 173.
[77] D. Zhao, P. Yang, N. Melosh, J. Feng, B. F. Chmelka, G. D. Stucky, *Adv. Mater.* **1998**, *10*, 1380 – 1385.
[78] J. M. Esparza, M. L. Ojeda, A. Campero, G. Hernández, C. Felipe, M. Asomoza, S. Cordero, I. Kornhauser, F. Rojas, *J. Mol. Catal. A* **2005**, *228*, 978 – 110.
[79] V. Bustos-Terrones, C. Menchaca, M. Romero Romo, J. M. Esparza, A. Domínguez, J. Uruchurtu, *Innovations in Corrosion and Material Science* **2015**, *5*, 31 – 35.
[80] http://www.chm.bris.ac.uk/motm/mcm41/mcm41.htm.
[81] E. F. Vansant, V. Van Der, K. C. Vrancken, **1995**, *Characterization and Chemical Modification of the Silica Surface*, Studies in Surf. Sci. and Catalysis. B. Delmon, J. T. Yates Editors, Vol. 93, Elsevier Cp. 4, 79 – 91.
[82] M. R. Caira, K. A. Alkhamis, R. M. Obaidat, *J. Pharm. Sci.* **2004**, *93*, 601 – 611.
[83] M. Karanam, S. Dev, A. R. Choudhury, *Cryst. Growth Des.* **2011**, *12*, 240 – 252.
[84] A. Pedretti, L. Villa, G. Vistoli, *J. Mol. Graphics Modell.* **2002**, *21*, 47 – 49.
[85] I. T. Weber, R. W. Harrison, *Protein Sci.* **1997**, *6*, 2365 – 2374.
[86] M. D. Hanwell, D. E. Curtis, D. C. Lonie, T. Vandermeersch, E. Zurek, G. R. Hutchison, *J. Cheminf.* **2012**, *4 – 17*, 17.
[87] A. K. Rappé, C. J. Casewit, K. S. Colwell, W. A. Goddard III, W. M. Skiff, *J. Am. Chem. Soc.* **1992**, *114*, 10024 – 10035.
[88] M. Valiev, E. J. Bylaska, N. Govind, K. Kowalski, T. P. Straatsma, H. J. Van Dam, D. Weng, J. Nieplocha, E. Apra, T. L. Windus, W. A. De Jong, *Comput. Phys. Commun.* **2010**, *181*, 1477 – 1489.
[89] K. Lira-De León, P. García-Gutiérrez, I. N. Serratos, M. Palomera-Cárdenas, M. D. P. Figueroa-Corona, V. Campos-Peña, M. A. Meraz-Ríos, *J. Alzheimer's Dis.* **2013**, *35*, 319 – 334.
[90] F. Reyes-Espinosa, A. Arroyo-Reyna, P. García-Gutiérrez, I. N. Serratos, R. A. Zubillaga, *Protein Pept. Lett.* **2014**, *22*, 239 – 247.
[91] A. I. Moral-Rodríguez, R. Leyva-Ramo, R. Ocampo-Pérez, J. Mendoza-Barron, I. N. Serratos-Alvarez, J. J. Salazar-Rabago, *Adsorption* **2016**, *22*, 89 – 103.
[92] V. Bustos-Terrones, I. N. Serratos, N. Castañeda-Villa, J. O. Vicente Escobar, M. A. Romero-Romo, J. Córdoba, J. Uruchurtu, C. Menchaca, J. M. Esparza, A. Domínguez, *Prog. Org. Coat.* **2018**, *119*, 221 – 229.
[93] M. R. Vengatesan, S. Devaraju, K. Dinakaran, M. Alagar, *J. Mater. Chem.* **2012**, *15*, 7559 – 7566.
[94] O. Trott, A. J. Olson, *J. Comput. Chem.* **2010**, *31*, 455 – 461.
[95] N. A. Baker, D. Sept, S. Joseph, M. J. Holst, J. A. McCammon, *Proc. Natl. Acad. Sci. USA* **2001**, *98*, 10037 – 10041.
[96] W. Humphrey, A. Dalke, K. Schulten, *J. Mol. Graphics* **1996**, *14*, 33 – 38.
[97] R. Hernández-Esparza, S. M. Mejía-Chica, A. D. Zapata-Escobar, A. Guevara-García, A. Martínez-Melchor, J. M. Hernández-Pérez, R. Vargas, J. Garza, *J. Comput. Chem.* **2014**, *35*, 2272 – 227.

Received: September 25, 2018
Revised manuscript received: October 23, 2018

